Science Advances
AAAS

Supplementary Materials for

Elastic turbulence generates anomalous flow resistance in porous media

Christopher A. Browne and Sujit S. Datta*

*Corresponding author. Email: ssdatta@princeton.edu

Published 5 November 2021, *Sci. Adv.* **7**, eabj2619 (2021)
DOI: 10.1126/sciadv.abj2619

The PDF file includes:

Supplementary text
Legends for movies S1 to S5
Figs. S1 to S12
Table S1
References

Other Supplementary Material for this manuscript includes the following:

Movies S1 to S5

Supplementary Materials

A Analysis of pore-scale flow

A.1 Processing of PIV data

In our analysis of the pore-scale flow, the root mean square velocity of a pixel is calculated as the temporal root mean square of the magnitude of the fluctuation from the temporal mean (*67*), $u_{\mathrm{rms}}(\mathbf{x}) = (\langle\|\mathbf{u}(\mathbf{x},t) - \langle\mathbf{u}(\mathbf{x},t)\rangle_t\|^2\rangle_t)^{1/2}$. We normalize this quantity by the velocity magnitude averaged over time and space (over all pixels) for each pore, $\langle u\rangle_{t,\mathbf{x}} = \langle\langle\|\mathbf{u}(\mathbf{x},t)\|\rangle_t\rangle_{\mathbf{x}}$. To quantify velocity fluctuations arising from unstable flow, we compute the velocity fluctuations $\mathbf{u}'(\mathbf{x},t) = \mathbf{u}(\mathbf{x},t) - \langle\mathbf{u}(\mathbf{x},t)\rangle_t$. This fluctuation field enables us to calculate the velocity gradient tensor associated with flow fluctuations, $s'_{ij} = \partial u'_i/\partial x_j$, pixel-by-pixel. In general, to compute the discrete derivatives, we use the central difference method, in which the derivative of f with respect to x evaluated around $x = x_0$ is given by

$$\left(\frac{\partial f}{\partial x}\right)_{x_0} \approx \frac{1}{2}\left(\frac{f(x_0+\Delta x) - f(x_0)}{\Delta x} + \frac{f(x_0) - f(x_0-\Delta x)}{\Delta x}\right).$$

On the boundaries of data sets, this central difference is replaced with the forward or backward finite difference (first or second term respectively).

A.2 Distributions of key flow parameters

To characterize the distribution of key flow parameters in the porous medium in the stable laminar case, we use our PIV measurements well below the onset of elastic turbulence (at $\dot{\gamma}_I = 0.48\ \mathrm{s}^{-1}$) to determine the base laminar flow field throughout the pore space. We then estimate the shear rate $\dot{\gamma} = \left(\partial u_i/\partial x_j + \partial u_j/\partial x_i\right)/3$ using the in-plane component $\dot{\gamma} \approx \partial u/\partial y + \partial v/\partial x$, since our 2D PIV cannot resolve out-of-plane velocity components. This approximation then allows us to estimate the magnitude of the spatially-varying Weissenberg number $\mathrm{Wi}(\mathbf{x}) \equiv N_1(\dot{\gamma}(\mathbf{x}))/2\sigma(\dot{\gamma}(\mathbf{x}))$ pixel-by-pixel using the rheologically-measured N_1 and σ. The distribution of the measured $\mathrm{Wi}(\mathbf{x})$ for 19 imaged pores is shown in Fig. S8A. As shown by the data, the characteristic interstitial Weissenberg number $\mathrm{Wi}_I \equiv N_1(\dot{\gamma}_I)/2\sigma(\dot{\gamma}_I)$ defined using imposed macroscopic flow conditions and macroscopic characteristics of the porous medium represents the upper limit of this distribution.

Elastic instabilities have been studied in a range of simplified geometries, and are typically parametrized using the Weissenberg number (*19–33, 40, 63, 68–82*). Thus, we also parametrize the different flow rates tested primarily using the Weissenberg number; however, we note that the onset of unstable flow due to streamline curvature can be described using a linear stability analysis of the Stokes equation for a viscoelastic fluid (*23, 68*). This analysis indicates that the largest destabilizing term, which leads to the generation of unstable flow locally, is proportional to $\mathrm{M} \equiv \sqrt{\mathrm{Wi} \cdot \mathrm{De}}$, where the Deborah number $\mathrm{De} \equiv \lambda(\dot{\gamma})||\mathbf{u}||\kappa$ compares the polymer relaxation time λ to the flow time scale $(||\mathbf{u}||\kappa)^{-1}$ and κ is a measure of the local streamline curvature (*20*). In this picture, elastic stresses build up in the flow, generating elastic turbulence when M exceeds a critical value M_c, found to be ≈ 6 to 20 in experiments performed in diverse simplified geometries (*20, 23, 26, 31, 68, 83, 84*). Thus, the transition to elastic turbulence could also be parameterized using a characteristic interstitial $\mathrm{M}_I \equiv \sqrt{\frac{N_1(\dot{\gamma}_I)}{\eta_0\dot{\gamma}_I} \cdot \lambda(\dot{\gamma}_I)(Q/A)\kappa_I}$, again defined using imposed macroscopic flow conditions and macroscopic characteristics of the porous medium; here the characteristic streamline curvature is set by the pore length scale, with $\kappa_I = 1/\left(2\sqrt{\phi k}\right)$. We again use our measurements of the spatially-varying shear rate $\dot{\gamma}(\mathbf{x})$, as well as direct measurements of the spatially-varying local streamline curvature $\kappa(\mathbf{x})$, to compute the spatially-varying $\mathrm{M}(\mathbf{x}) = \sqrt{\mathrm{Wi}(\mathbf{x}) \cdot \mathrm{De}(\mathbf{x})}$, pixel-by-pixel. The distribution of the measured $\mathrm{M}(\mathbf{x})$ for all 19 imaged pores is shown in Fig. S8B. As shown by the data, the characteristic interstitial M_I defined using imposed macroscopic flow conditions and macroscopic characteristics of the porous medium represents the upper limit of this distribution. For our experiments, M_I ranges from 3.3 to 8.1. The range of $\mathrm{M}_{c,i}$ at which pores become unstable is measured to be ≈ 5.5 to

7.9, in good agreement with the range of ≈ 6 to 20 observed in simplified geometries.

A.3 Determination of pore-scale critical Weissenberg number

To determine the critical Weissenberg number in each pore, we first plot the fraction of time unstable F_t for each pore. To superpose the plots, we shift each curve by the Wi_{50}, defined by the point where $F_t = 0.5$, linearly interpolating between data points as needed: this procedure enables us to avoid noise in the limits $F_t \approx 0$ and $F_t \approx 1$. We define a constant shift of $\mathrm{Wi}_c = \mathrm{Wi}_{50} - 0.35$ (Table S1), which minimizes the error in the power law fit $F_t \sim (\mathrm{Wi}_I/\mathrm{Wi}_c - 1)^{\alpha_f}$, where the exponent $\alpha_f \approx 0.4 \pm 0.1$ is obtained from the best fit across all pores. Pores where Wi_c is ambiguous are omitted from this fit and the distribution shown in Fig. 2E-F.

B Power density balance

We start with the scalar partial differential equation for the rate of change of mechanical energy per unit volume, obtained by dotting the Cauchy momentum equation with velocity (*85*):

$$\frac{\partial}{\partial t}\left(\frac{1}{2}\rho u^2\right) + \nabla \cdot \frac{1}{2}\rho u^2 \mathbf{u} - P\nabla \cdot \mathbf{u} + \nabla \cdot [\boldsymbol{\tau} \cdot \mathbf{u}] - \rho \mathbf{u} \cdot \mathbf{g} = -\nabla \cdot P\mathbf{u} - \boldsymbol{\tau} : \nabla \mathbf{u}, \tag{S1}$$

where $\mathbf{u}(\mathbf{x}, t)$ is the fluid velocity, ρ is the fluid density, $P(\mathbf{x}, t)$ is the fluid pressure, $\boldsymbol{\tau}(\mathbf{x}, t)$ is the fluid stress tensor, and $\mathbf{g}$ is gravitational acceleration.

The first term $\frac{\partial}{\partial t}\left(\frac{1}{2}\rho u^2\right)$ represents the change in kinetic energy, which is of order Re and thus negligible. The second term $\nabla \cdot \frac{1}{2}\rho u^2 \mathbf{u}$ represents the acceleration over a control volume; this term disappears, since the inlet and outlet of our capillary have the same surface area, so there is no acceleration across the medium. The third term $P\nabla \cdot \mathbf{u}$ represents the reversible work of compression, which is negligible for an incompressible fluid $\nabla \cdot \mathbf{u} = 0$. The fourth term $\nabla \cdot [\boldsymbol{\tau} \cdot \mathbf{u}]$ represents viscous work done across control surfaces; this term disappears, since there is no viscous work done at the capillary walls and the flow is unidirectional across the inlet and outlet control surfaces. The fifth term $\rho\mathbf{u}\cdot\mathbf{g}$ represents gravitational work done, which scales with the Reynolds and Froude numbers: $\rho\mathbf{u}\cdot\mathbf{g} \sim \mathrm{Re}/\mathrm{Fr}^2 = \rho g D_p^2/\eta_0 \approx 0.0028 \ll 1$ and is thus negligible. This leaves only the last two terms for our experiments:

$$-\nabla\cdot P\mathbf{u} = \boldsymbol{\tau} : \nabla\mathbf{u}. \tag{S2}$$

The left hand side represents the rate of work done by the fluid pressure and the right hand side represents the rate of viscous energy dissipation, per unit volume. The velocity gradient tensor can be decomposed into a symmetric and asymmetric component $\nabla\mathbf{u} = \mathbf{s} + \boldsymbol{\omega}$, where $\mathbf{s} = (\nabla\mathbf{u} + \nabla\mathbf{u}^{\mathrm{T}})/2$ is the rate of strain tensor and $\boldsymbol{\omega} = (\nabla\mathbf{u} - \nabla\mathbf{u}^{\mathrm{T}})/2$ is the vorticity tensor.

B.1 Macroscopic averaging

Taking the volume integral of Eq. S2 and applying the divergence theorem to the left hand side yields the macroscopic power balance over the control volume. This volume is composed of the four capillary walls and a surface perpendicular to the walls well upstream and downstream of the bead packing, such that the flow is unidirectional $\mathbf{u} = u_x\hat{\mathbf{x}}$ across the inlet/outlet surfaces $\mathbf{n} = \pm\hat{\mathbf{x}}$:

$$\begin{aligned} -\int_{\mathscr{A}} P\mathbf{u}\cdot\mathbf{n}\mathrm{d}A &= \int_V \boldsymbol{\tau} : (\mathbf{s}+\boldsymbol{\omega})\mathrm{d}V \\ \Longrightarrow\ (Q/A)A\Delta P &= V\langle\boldsymbol{\tau} : (\mathbf{s}+\boldsymbol{\omega})\rangle_V \\ \Longrightarrow\ \frac{\Delta P}{\Delta L} &= \frac{\langle\boldsymbol{\tau} : (\mathbf{s}+\boldsymbol{\omega})\rangle_V}{Q/A}. \end{aligned} \tag{S3}$$

B.2 Time averaging

Drawing inspiration from the treatment of inertial turbulence, in which flows similarly exhibit strong spatio-temporal fluctuations, we decompose the velocity into a time-averaged and a fluctuating component $\mathbf{u}(\mathbf{x},t) = \mathbf{u}_0(\mathbf{x}) + \mathbf{u}'(\mathbf{x},t)$, from which it follows that the rate of strain and vorticity tensors also decompose $\mathbf{s}(\mathbf{x},t) = \mathbf{s}_0(\mathbf{x}) + \mathbf{s}'(\mathbf{x},t)$ and $\boldsymbol{\omega}(\mathbf{x},t) = \boldsymbol{\omega}_0(\mathbf{x}) + \boldsymbol{\omega}'(\mathbf{x},t)$. The pressure similarly decomposes into a mean and fluctuating component $P(\mathbf{x}, t) = P_0(\mathbf{x}) + P'(\mathbf{x}, t)$, with $\langle P' \rangle_t = 0$ and thus $\langle P \rangle_t = P_0$. The time-averaged pressure drop is obtained by taking the time average $\langle\ \ \rangle_t = \frac{1}{t_c}\int_{-t_c/2}^{+t_c/2}(\ \ )\mathrm{d}t$ of Eq. S3 over a moving window $t = \pm t_c/2$, where t_c is a sufficiently large time window for meaningful averaging (*86*):

$$\frac{\langle \Delta P \rangle_t}{\Delta L} = \frac{\langle\langle \boldsymbol{\tau} : (\mathbf{s} + \boldsymbol{\omega})\rangle_t\rangle_V}{Q/A}. \tag{S4}$$

Evaluating the right hand side of this equation requires knowledge of the full dependence of the stress τ on polymer strain history in 3D (*47*), which is currently inaccessible in our experiments. However, motivated by the observations that the flow is quasi-steady and does not appreciably accumulate strain over a polymer relaxation time, we use a generalized Newtonian fluid model in which the stress depends on a nonlinear extensional viscosity η_e, which incorporates the strain history of the quasi-steady flow, and on a nonlinear shear viscosity η_s, depending on the local flow field.

We then decompose the dissipation function $\langle \boldsymbol{\tau} : \nabla \mathbf{u} \rangle_t$ into a mean and fluctuating component. Because our calculations of Hencky strain (described in the Materials and Methods of the main text) suggest that extensional viscosity does not appreciably contribute to the global viscous dissipation, we express the fluid stress as a function of the local rate of strain tensor, $\tau_{ij}(s_{ij})$ (*38*). Since the stress is nonlinear for a non-Newtonian fluid, the function for stress $\tau_{ij}(s_{0,ij} + s'_{ij})$ cannot easily be separated into a mean and fluctuating term; instead, we expand τ_{ij} with a Maclaurin series, applying the definition of fluctuations $\langle s'_{ij} \rangle_t \equiv 0$ and $\langle \omega'_{ij} \rangle_t \equiv 0$, but

$\langle s_{ij}'^2 \rangle_t \neq 0$:

$$
\begin{aligned}
&\langle \tau_{ij}|_{s_{0,ij}+s'_{ij}} (s_{ij} + \omega_{ij}) \rangle_t \\
&\quad = \left\langle \left(\tau_{ij}|_{s_{0,ij}} + \frac{\partial \tau_{ij}}{\partial s_{ij}}\bigg|_{s_{0,ij}} s'_{ij} + \frac{1}{2}\frac{\partial^2 \tau_{ij}}{\partial s_{ij}^2}\bigg|_{s_{0,ij}} s_{ij}'^2 + \frac{1}{3}\frac{\partial^3 \tau_{ij}}{\partial s_{ij}^3}\bigg|_{s_{0,ij}} s_{ij}'^3 + \mathscr{O}(s_{ij}'^4) \right) (s_{0,ij} + \omega_{0,ij} + s'_{ij} + \omega'_{ij}) \right\rangle_t \\
&\quad = \underbrace{\tau_{ij}|_{s_{0,ij}} (s_{0,ij} + \omega_{0,ij})}_{\text{Mean flow: Darcy}} + \underbrace{\left[\frac{\partial \tau_{ij}}{\partial s_{ij}}\bigg|_{s_{0,ij}} + \frac{s_{0,ij} + \omega_{0,ij}}{2} \frac{\partial^2 \tau_{ij}}{\partial s_{ij}^2}\bigg|_{s_{0,ij}} \right] \langle s_{ij}'^2 \rangle_t}_{\text{Unstable flow: } \langle \chi \rangle_t} + \mathscr{O}(\langle s_{ij}'^4 \rangle_t),
\end{aligned}
\tag{S5}
$$

which is accurate to fourth order $\mathscr{O}(\langle s_{ij}'^4 \rangle_t)$. The first term reflects the viscous dissipation of the mean flow, ultimately yielding Darcy's law when volume averaged, by definition: $\langle \tau_{ij}|_{s_{0,ij}} (s_{0,ij} + \omega_{0,ij}) \rangle_V / (Q/A) = \eta(\dot{\gamma}_I)(Q/A)/k$. The second term reflects viscous dissipation due to unstable flow fluctuations, and we define it as the rate of added dissipation $\langle \chi \rangle_t$.

B.3 Unstable dissipation function

The term in square brackets in Eq. S5 has units of a dynamic viscosity, prompting the *ansatz* that it should be proportional to $\eta(\dot{\gamma}_0)$, where $\dot{\gamma}_0 \equiv 2 s_{0,xy} = \partial u_0/\partial y + \partial v_0/\partial x$ and c_{ij} is the proportionality constant:

$$
\begin{aligned}
\langle \chi \rangle_t &\equiv \left[\frac{\partial \tau_{ij}}{\partial s_{ij}}\bigg|_{s_{0,ij}} + \frac{s_{0,ij} + \omega_{0,ij}}{2} \frac{\partial^2 \tau_{ij}}{\partial s_{ij}^2}\bigg|_{s_{0,ij}} \right] \langle s_{ij}'^2 \rangle_t \\
&\equiv c_{ij} \eta(\dot{\gamma}_0) \langle s_{ij}'^2 \rangle_t.
\end{aligned}
\tag{S6}
$$

For a power-law fluid, $\tau_{ij} = A_s (s_{ij})^{\alpha_s}$, where A_s and α_s are material constants. This constitutive relationship allows us to compute c_{ij}:

$$
\begin{aligned}
c_{ij} \eta(\dot{\gamma}_0) &\equiv \frac{\partial \tau_{ij}}{\partial s_{ij}}\bigg|_{s_{0,ij}} + \frac{s_{0,ij} + \omega_{0,ij}}{2} \frac{\partial^2 \tau_{ij}}{\partial s_{ij}^2}\bigg|_{s_{0,ij}} \\
&= \alpha_s A_s s_{0,ij}^{\alpha_s - 1} \left(1 + \frac{s_{0,ij} + \omega_{0,ij}}{s_{0,ij}} \frac{(\alpha_s - 1)}{2} \right) \\
&= \alpha_s 2^{1-\alpha_s} \left(1 - (1 + \Lambda_{ij}) \frac{(1 - \alpha_s)}{2} \right) \eta(\dot{\gamma}_0),
\end{aligned}
\tag{S7}
$$

where, assuming isotropic unstable flow fluctuations, $\eta(s_{0,ij}) \approx \eta(s_{0,xy}) \equiv \eta(\dot{\gamma}_0/2)$.

The term $\Lambda_{ij} \equiv \omega_{0,ij}/s_{0,ij}$ cannot be directly measured from a 2D flow field; simple averaging for the unknown elements in the third direction k would trivially return $\Lambda_{ik} = 0$. However, estimating the magnitude of Λ_{ij} using just the in-plane component indicates that the entire term is typically much less than order one: averaging over all pixels and flow rates yields $\langle(1 + \Lambda_{ij})(\alpha_s - 1)/2\rangle_{V,Q} = 0.026 \ll 1$, as shown in Fig. S11. We therefore neglect this term. Thus, $c = \alpha_s 2^{1-\alpha_s}$; $c = 1$ for a Newtonian fluid and $0 < c < 1$ for shear-thinning fluids. Using our measured fluid rheology, we find $c = 0.98$—reflecting that our fluid has nearly constant shear viscosity for the shear rates tested.

The unstable dissipation function $\langle\chi\rangle_t$ then depends primarily on the fluctuating rate of strain tensor $\langle s_{ij}'^2\rangle_t$. Again assuming isotropic flow fluctuations, as is frequently done in the case of inertial turbulence (*87, 88*),

$$\begin{aligned}
\left\langle\left(\frac{\partial u_z'}{\partial z}\right)^2\right\rangle_t &\approx \frac{1}{2}\left[\left\langle\left(\frac{\partial u_x'}{\partial x}\right)^2\right\rangle_t + \left\langle\left(\frac{\partial u_y'}{\partial y}\right)^2\right\rangle_t\right] \\
\left\langle\left(\frac{\partial u_x'}{\partial z}\right)^2\right\rangle_t &\approx \left\langle\left(\frac{\partial u_y'}{\partial z}\right)^2\right\rangle_t \approx \left\langle\left(\frac{\partial u_z'}{\partial x}\right)^2\right\rangle_t \approx \left\langle\left(\frac{\partial u_z'}{\partial y}\right)^2\right\rangle_t \\
&\approx \frac{1}{2}\left[\left\langle\left(\frac{\partial u_x'}{\partial y}\right)^2\right\rangle_t + \left\langle\left(\frac{\partial u_y'}{\partial x}\right)^2\right\rangle_t\right] \\
\left\langle\left(\frac{\partial u_x'}{\partial z}\frac{\partial u_z'}{\partial x}\right)\right\rangle_t &\approx \left\langle\left(\frac{\partial u_y'}{\partial z}\frac{\partial u_z'}{\partial y}\right)\right\rangle_t \\
&\approx -\frac{1}{4}\left[\left\langle\left(\frac{\partial u_x'}{\partial x}\right)^2\right\rangle_t + \left\langle\left(\frac{\partial u_y'}{\partial y}\right)^2\right\rangle_t\right]
\end{aligned}$$

$$\begin{aligned}
\implies \langle\chi\rangle_t &\equiv c\eta(\dot\gamma_0)\langle s_{ij}'^2\rangle_t \\
&\approx c\eta(\dot\gamma_0)\left[2\left\langle\left(\frac{\partial u_x'}{\partial x}\right)^2\right\rangle_t + 2\left\langle\left(\frac{\partial u_y'}{\partial y}\right)^2\right\rangle_t + 3\left\langle\left(\frac{\partial u_y'}{\partial x}\right)^2\right\rangle_t + 3\left\langle\left(\frac{\partial u_x'}{\partial y}\right)^2\right\rangle_t + 2\left\langle\frac{\partial u_y'}{\partial x}\frac{\partial u_x'}{\partial y}\right\rangle_t\right]. \quad \text{(S8)}
\end{aligned}$$

This quantity, which quantifies the rate of added viscous dissipation due to unstable flow fluctuations, can now be fully determined from our PIV measurements. In the main text, we write this in the form $\langle\chi\rangle_t \approx \eta\langle\mathbf{s}' : \mathbf{s}'\rangle_t$ for simplicity, and our computations use the full form shown in Eq. S8.

B.4 Apparent viscosity

Having computed the unstable dissipation rate $\langle\chi\rangle_t$ using our direct pore-scale flow visualization, *via* Eq. S8, we use this quantity to determine the overall apparent viscosity of the flowing polymer solution. First, we directly compute $\langle\chi\rangle_{t,V}$ by averaging $\langle\chi\rangle_t$ over the imaged area of each pore, and then averaging over all the imaged pores. Above the critical global Weissenberg number $\mathrm{Wi}_c = 2.6$, $\langle\chi\rangle_{t,V}$ increases sharply with an apparent power law scaling $\langle\chi\rangle_{t,V} = A_x(\mathrm{Wi}/\mathrm{Wi}_c - 1)^{\alpha_x}$. We fit $A_x = 279 \pm 1$ W/m^3 and $\alpha_x = 2.6 \pm 0.4$, as shown in Fig. 4B of the main text. Then, we substitute $\langle\chi\rangle_{t,V}$ into Eqs. S4-S5 to obtain our final result:

$$\begin{aligned}
\frac{\langle\Delta P\rangle_t}{\Delta L} &= \frac{\langle \boldsymbol{\tau}|_{\mathrm{s}_0} : \nabla\mathbf{u}_0\rangle_V}{Q/A} + \frac{\langle\chi\rangle_{t,V}}{Q/A} \\
&= \frac{\eta(\dot{\gamma}_I)Q/A}{k} + \frac{\langle\chi\rangle_{t,V}}{Q/A} \\
\implies \eta_{\mathrm{app}}(\dot{\gamma}_I) &= \eta(\dot{\gamma}_I) + \frac{k\langle\chi\rangle_{t,V}}{(Q/A)^2}.
\end{aligned} \tag{S9}$$

B.5 Origin of the peak in $\eta_{\mathrm{app}}(\mathrm{Wi}_I)$

The power balance quantified by Eq. S9 yields a peak in $\eta_{\mathrm{app}}(\mathrm{Wi}_I)$, in good agreement with the experimental measurements, as shown in Fig. 4C of the main text. As described below, this peak reflects the Wi_I-dependence of the dissipation rate of chaotic flow fluctuations $\langle\chi\rangle_{t,V} \sim (\mathrm{Wi}_I/\mathrm{Wi}_c - 1)^{\alpha_x}$. In particular, to have a peak in $\eta_{\mathrm{app}}(\mathrm{Wi}_I)$ at $\mathrm{Wi}_I = \mathrm{Wi}_p > \mathrm{Wi}_c$,

$$\begin{aligned}
0 &= \frac{\mathrm{d}}{\mathrm{d}(\mathrm{Wi}_I)}\left.\frac{\langle\chi\rangle_{t,V}}{(Q/A)^2}\right)_{\mathrm{Wi}_p} \\
0 &= \frac{\mathrm{d}}{\mathrm{d}(\mathrm{Wi}_I)}\left.\frac{(\mathrm{Wi}_I - \mathrm{Wi}_c)^{\alpha_x}}{\mathrm{Wi}_I^{2/(\alpha_n-\alpha_s)}}\right)_{\mathrm{Wi}_p} \\
\implies \mathrm{Wi}_p &= \frac{2\mathrm{Wi}_c}{2 - \alpha_x(\alpha_n - \alpha_s)}.
\end{aligned} \tag{S10}$$

where in the second line we have applied the definition of the Weissenberg number and the measured rheological relationships shown in Fig. S1, which yield $Q \sim \dot{\gamma}_I \sim \mathrm{Wi}_I^{1/(\alpha_n-\alpha_s)}$. Thus, we expect that the measured apparent viscosity will anomalously increase beyond the Darcian baseline for $\mathrm{Wi} > \mathrm{Wi}_c$ and will peak when $\mathrm{Wi} = \mathrm{Wi}_p$ as given above. Fitting our experimental data yields $\mathrm{Wi}_c = 2.6$, $\alpha_x = 2.6$, $\alpha_n = 1.23$, $\alpha_s = 0.934$, yielding a predicted peak at $\mathrm{Wi}_I = \mathrm{Wi}_p = 4.4$, in excellent agreement with our measured $\mathrm{Wi}_{c,max} = 4.4$. For even larger $\mathrm{Wi}_I > \mathrm{Wi}_p$, the dissipation rate due to chaotic flow fluctuations $\langle\chi\rangle_{t,V}$ does not increase with Wi_I as quickly as $(Q/A)^2$, and our analysis suggests that η_{app} decays back to η — indicating that the viscous dissipation associated with the base laminar flow increasingly dominates, although strain history effects, inertia, and chain scission will likely also play a role in this regime. Investigating these high Wi_I effects, and more generally investigating the underpinnings of the dependence of $\langle\chi\rangle_{t,V}$ on Wi_I, will be a useful direction for future research.

B.6 Upper bound estimate for the contribution from strain history effects

Motivated by our observation that most of the unstable flow fluctuations are slow (on time scales longer than λ), we develop an upper bound estimate of the last term in Eq. 3 of the main text. In general, this is history dependent, but we expect that it will be bounded by the steady state extensional viscosity expected for the polymer solution. In particular, the additional polymer contribution to extensional viscosity $\eta_{e,p}$ should add a third term to the right hand side of Eq. S9:

$$\frac{k\langle\eta_{e,p}\dot{\varepsilon}^2\rangle_{t,V}}{(Q/A)^2}, \tag{S12}$$

where as a strict upper bound, we take $\mathrm{Tr} \longrightarrow 1000$ or $\eta_{e,p} \sim 10^3\eta_0$ (*48*). Following previous work (*10, 12*), we estimate the characteristic extensional rate as $\dot{\varepsilon} \approx Q/(\phi_V A)/D_p \sim 0.1$ to $0.6\ \mathrm{s}^{-1}$ in our experiments, where D_p is the mean bead diameter. Given that our measurements of Hencky strain indicate negligible extension in the pore bodies, we approximate the fraction of the total volume over which the maximal extension takes place as $d_t^3/\left(d_t^3 + d_b^3\right)$, where $d_t = 0.16D_p$ and $d_b = 0.24D_p$ are the pore throat and body diameters for a bead packing, respectively. Thus, we estimate $\langle \eta_{e,p}\dot{\varepsilon}^2\rangle_{t,V} \sim \left(10^3\eta_0\right)\left[Q/(\phi_V A)/D_p\right]^2\left[d_t^3/\left(d_t^3+d_b^3\right)\right] \sim 0.6$ to $20\ \mathrm{W/m^3}$. The entire term of Eq. S12 is then ~ 0.6 at all tested Wi_I. Adding this term as an upper bound to the model of Eq. S9 gives the green region in Figure S12. The actual additional contribution of polymer-induced extensional viscous dissipation should fall somewhere in this region, since Hencky strains are unlikely to actually reach this infinite extension limit. This neglected contribution of polymer extensional viscosity in the pore throats can thus likely account for the $\sim$ 10% discrepancy between our model in S9 and the peak in the apparent viscosity. Quantifying the exact role of this term requires modeling the full strain history of polymers in the unstable flow field, and will be an important direction for future work.

C Supplementary Movie Captions

Movie S1. Velocity field of example pore (pore B) just below onset of instability ($\dot{\gamma}_I = 2.6\ \mathrm{s}^{-1}$; $\mathrm{Wi}_I = 2.6$). Applied flow is left to right. Each frame is 4 min apart (720x speed). Arrows indicate the vector field, and colors indicate velocity magnitude as measured by particle image velocimetry (PIV). Velocities do not change appreciably over time above the error of PIV.

Movie S2. Velocity field of example pore (pore B) above onset of instability ($\dot{\gamma}_I = 7.3\ \mathrm{s}^{-1}$; $\mathrm{Wi}_I = 3.6$). Applied flow is left to right. Each frame is 4 min apart (720x speed). Arrows indicate the vector field, and colors indicate velocity magnitude as measured by particle image velocimetry (PIV). Velocities exhibit strong spatio-temporal fluctuations, consistent with the onset of an elastic instability.

Movie S3. Fluctuating velocity field of example pore (pore B) near cusp of instability ($\dot{\gamma}_I = 4.8\ \mathrm{s}^{-1}$; $\mathrm{Wi}_I = 3.2$). Applied flow is left to right. Each frame is 4 min apart (720x speed). Colors indicate fluctuating velocity magnitude as measured by particle image velocimetry (PIV). Right shows kymograph of fluctuating velocity field for an example column of pixels (marked by red lines). Puffs of fluctuations decay in time.

Movie S4. Fluctuating velocity field of example pore (pore B) well above onset of instability ($\dot{\gamma}_I = 9.7$ s^{-1}; $\mathrm{Wi}_I = 3.9$). Applied flow is left to right. Each frame is 4 min apart (720x speed). Colors indicate fluctuating velocity magnitude as measured by particle image velocimetry (PIV). Right shows kymograph of fluctuating velocity field for an example column of pixels (marked by red lines). Fluctuations are sustained in time.

Movie S5. Fluctuating velocity field of example pore (pore B) well above onset of instability ($\dot{\gamma}_I = 9.7$ s^{-1}; $\mathrm{Wi}_I = 3.9$) shown at high time resolution. Applied flow is left to right. Each PIV frame averaged over over 1/6 s. Video shown at 5x speed. Colors indicate fluctuating velocity magnitude as measured by particle image velocimetry (PIV). Right shows kymograph of fluctuating velocity field for an example column of pixels (marked by red lines). Fluctuations are sustained in time.

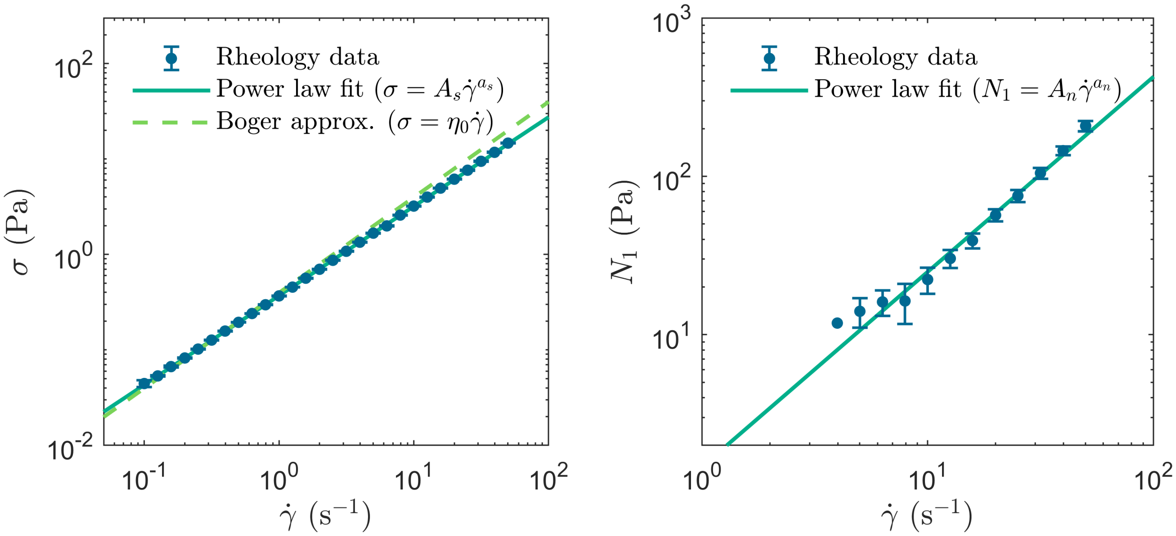

Figure S1: **Bulk rheology measurements of the shear stress and first normal stress difference as a function of shear rate for the polymer solution used in all experiments**. Error bars represent standard deviation over four samples. A power law fit for shear stress $\sigma(\dot{\gamma}) \approx A_s(\dot{\gamma})^{\alpha_s}$ gives $A_s \approx 0.369(8)$ Pa $\cdot$ $s^{1+\alpha_s}$, $\alpha_s \approx 0.934(7) \pm 0.001$. A power law fit for the first normal stress difference $N_1(\dot{\gamma}) \approx A_n(\dot{\gamma})^{\alpha_n}$ gives $A_n \approx 1.46(3)$ Pa $\cdot$ $s^{1+\alpha_n}$, $\alpha_n \approx 1.23(1) \pm 0.04$.

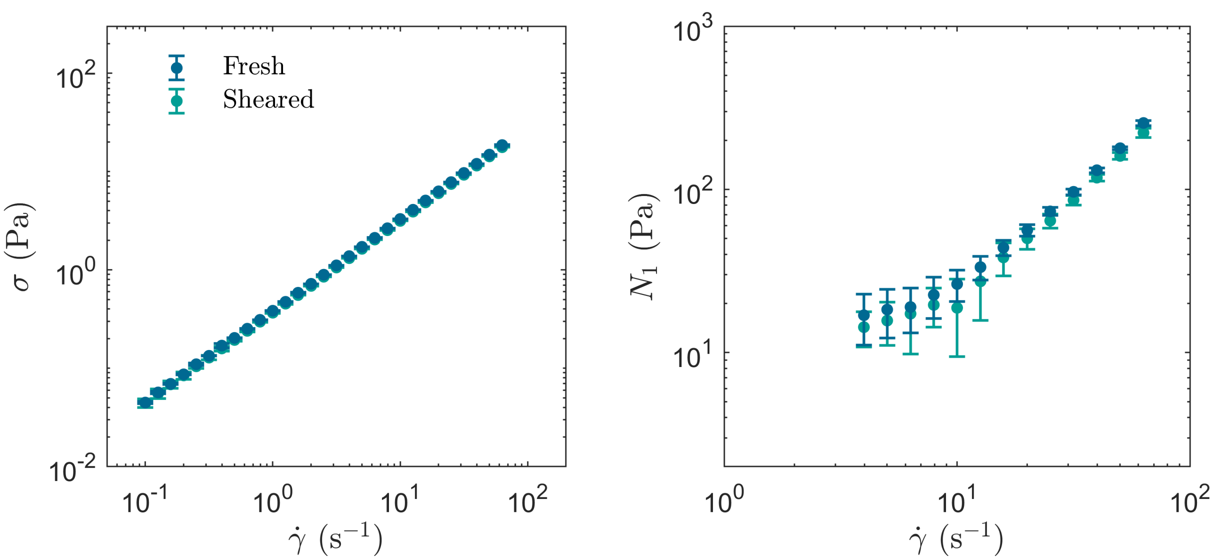

Figure S2: **Bulk rheology measurements of the same polymer solution before and after injection into the porous medium**. Comparison of rheology for fresh polymer solution and sheared polymer solution passed through the porous medium at highest tested flow rate of Q = 5 mL/hr. Error bars represent standard deviation over three replicate samples.

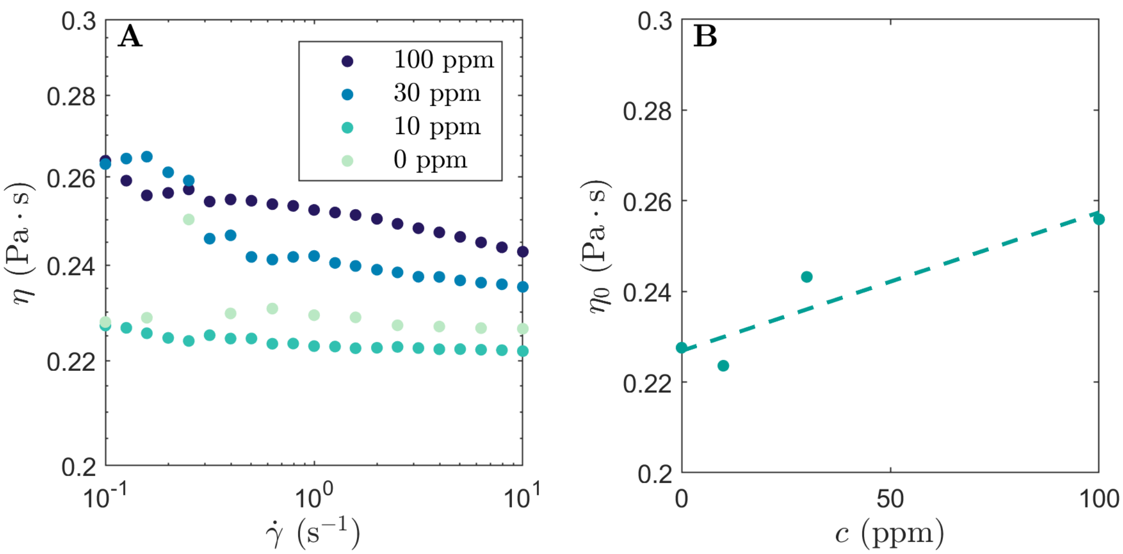

Figure S3: **Bulk rheology measurement of the solution intrinsic viscosity**. **A** Shear viscosity measurements of polymer solution diluted with pure solvent. **B** Fit of the measured zero-shear viscosity η_0 with concentration c gives $\eta_0/\eta_s = 1 + [\eta]c$ where the pure solvent viscosity is $\eta_s = 0.226 \pm 0.009$ Pa · s and the intrinsic viscosity is $[\eta] = (3 \pm 1) \times 10^{-4}$ ppm^{-1}.

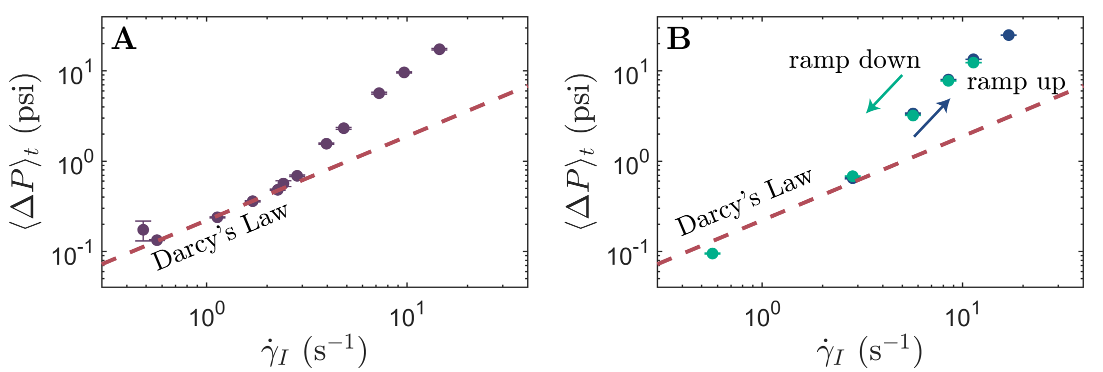

Figure S4: **Raw pressure drop data at different imposed flow rates**. **A** Time-averaged pressure drop data corresponding to Figs. 1B and 4C. Red dashed line shows the prediction of Darcy's Law using the shear viscosity of the bulk solution. Error bars represent one standard deviation of the pressure drop measurements taken over a 1 h measurement window; when not shown, error bars are smaller than the symbol size. **B** Pressure drop measurements taken while ramping up (dark blue) and down (light green) flow rate show no measurable hysteresis, similar to observations in model 2D porous media (*28, 35, 65*).

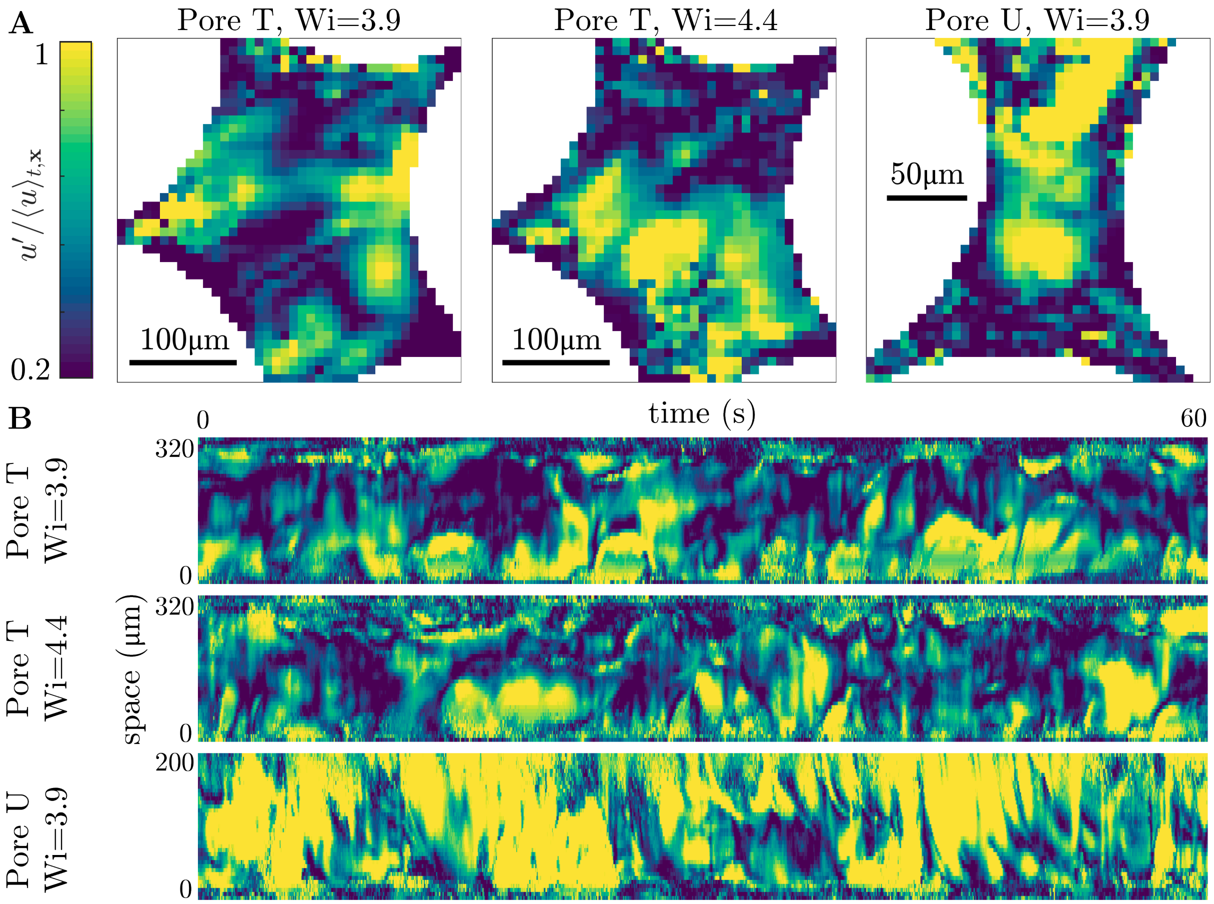

Figure S5: **Characterization of spatiotemporal fluctuations in flow velocity**. **A** Magnitude of velocity fluctuations u' normalized by the mean velocity $\langle u\rangle_{t,\mathbf{x}}$ for a pore at $\mathrm{Wi}_I = 3.9$, the same pore at $\mathrm{Wi}_I = 4.4$, and another pore at $\mathrm{Wi}_I = 3.9$. Pore labels are described in Table S1. **B** Accompanying kymograph of fluctuations taken from a vertical line along the center of each pore (spatially averaging 3 pixels in the x-direction). The PIV frame rate of 6 frames per second shows finer time resolution than Figs. 2A-D of the main text, allowing for the spectral analysis shown in Fig. S6.

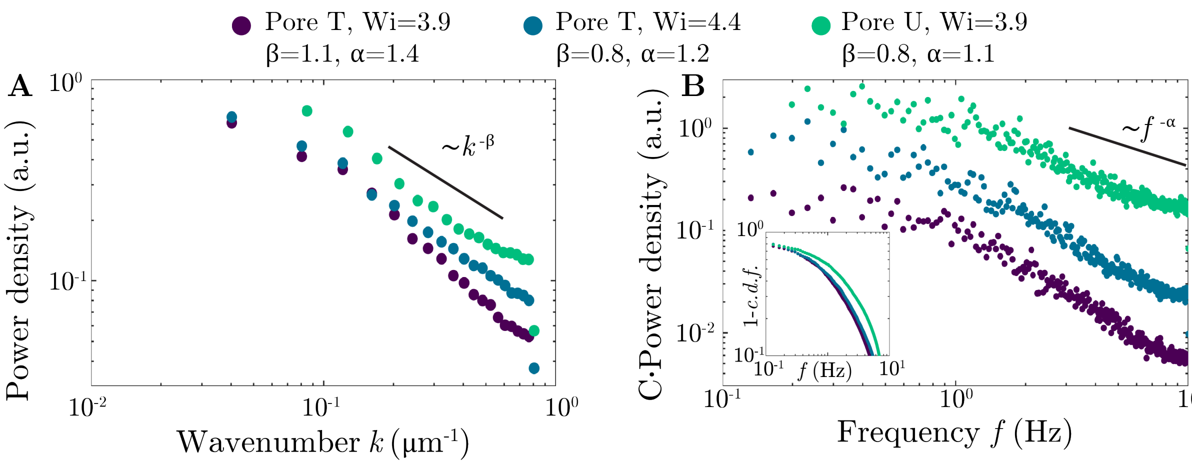

Figure S6: **Spatial and temporal power spectra of velocity fluctuations**. **A** The Fourier transform of the spatial signal $u'(x)$ averaged over the temporal points in the kymograph to smooth out noise. Best fit power-law scalings decay with wave numbers $\sim k^{-\beta}$ with $\beta \approx -0.8$ to 1.1, in agreement with the range $\beta \approx 1$ to 3 reported for elastic turbulence in various other geometries (*33, 40, 44, 63*). The upper wavenumbers are limited by the pixel size 0.62 μm, and the lower wavenumbers are limited by the frame size (200 or 320 μm). **B** The Fourier transform of the temporal signal $u'(t)$, averaged to smooth noise over 3 time points and a box of pixels taken from the center of the pore (10×7 for pore T, 5×13 for pore U), vertically shifted by a constant factor for clarity (C = 1 for pore T at $\mathrm{Wi}_I = 3.9$, C = 2 for pore T at $\mathrm{Wi}_I = 4.3$, C = 6 for pore U at $\mathrm{Wi}_I = 3.9$). Best fit power-law scalings decay with frequencies $\sim f^{-\alpha}$ with $\alpha = 1.1$ to 1.4. The upper frequency is capped at 2 Hz because of the PIV framerate and time averaging, and lower frequencies deviate $\lesssim$ .2 Hz because of the finite experiment duration. These scalings agree with the broad range of $\alpha \approx 1$ to 3.7 reported for elastic turbulence in various other geometries (*35, 36, 40, 44, 64–66*). Inset shows the complementary cumulative distribution function (*c.d.f.*) indicating that the majority of measured power spectral density is contained in fluctuations longer than one polymer relaxation time $\lambda \approx \mathrm{Wi}_I/\dot{\gamma}_I \approx 0.4$ s.

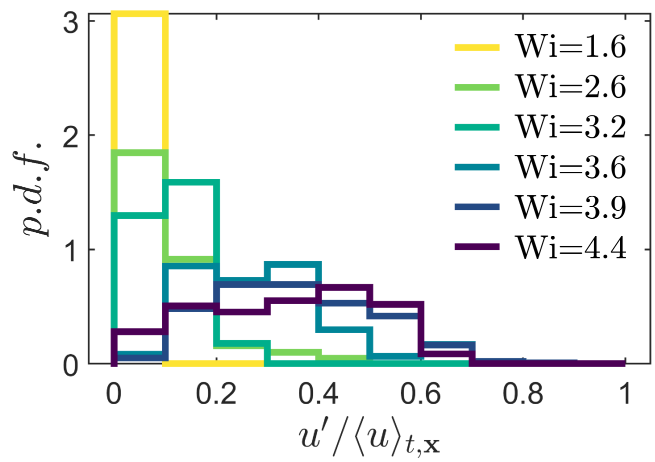

Figure S7: **Distribution of the magnitude of flow fluctuations u' normalized by the mean $\langle u\rangle_{t,\mathbf{x}}$ in a representative pore B at different imposed Weissenberg numbers**. For the laminar $\mathrm{Wi}_I = 1.6$, the fluctuations are contained near zero, representing experimental PIV noise. At higher Wi_I, the fluctuations grow in magnitude, and hence the persistence of bursts above our chosen threshold $u'/\langle u\rangle_{t,\mathbf{x}} > 0.2$ increase continuously.

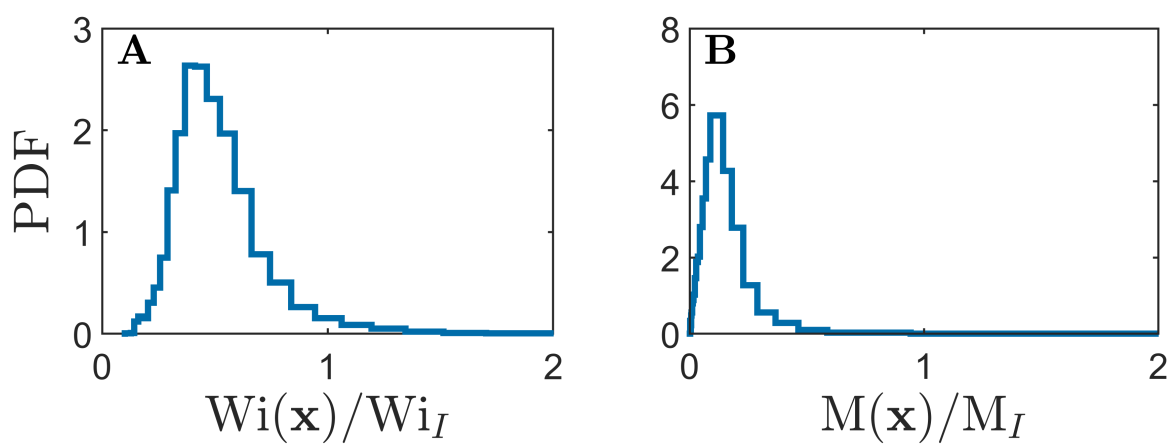

Figure S8: **Distributions of flow parameters for 19 imaged pores in the laminar steady flow regime**. **(A)** The local Wi is broadly distributed; the characteristic macroscopically-defined Wi_I represents the upper bound of this distribution. **(B)** The local M is also broadly distributed; the characteristic macroscopically-defined M_I represents the upper bound of this distribution.

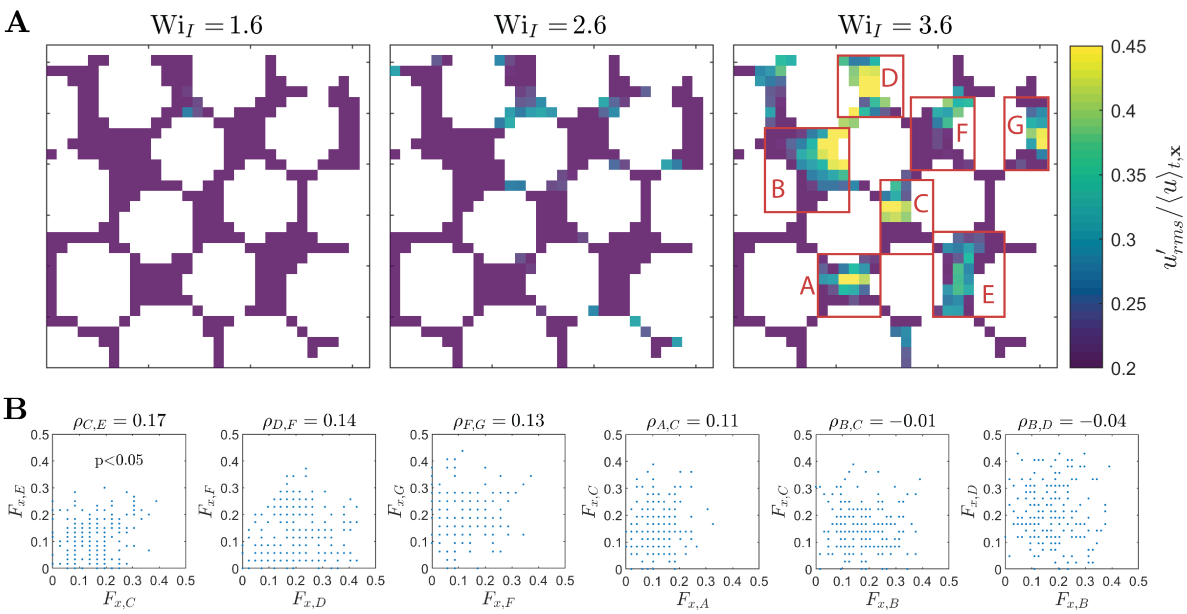

Figure S9: **Evaluating the possible role of flow correlations between neighboring pores**. **A** Multi-pore imaging at three different flow rates indicates that localized regions of unstable flow (blue, green, yellow) coexist amidst regions of stable flow (purple). **B** To quantify possible correlations in the flow across neighboring pores, we measure the temporal variation of the instantaneous fraction of space $F_{x,i}$ that is unstable ($u'/\langle u \rangle_{t,\mathbf{x}} > 0.2$, where $\langle u \rangle_{t,\mathbf{x}}$ is taken over the entire multi-pore field of view) in each pore i, and assess the correlation between the different $F_{x,i}$ at each time, indicated by each blue point in the panels shown. The pore labels i are indicated in the third panel of **A**. The Pearson correlation coefficients obtained from the data for pores i and j are indicated by $\rho_{i,j}$. Only one pair of neighboring pores (C and E) shows a statistically significant correlation ($p < 0.05$, two-tailed t-test), but only with a weak correlation of $\rho_{C,E} = 0.17$; all other pairs of pores show no significant correlation in flow state. Thus, unstable pores may be weakly correlated to their closest neighbors, but these unstable regions are fairly independent from pores further away — supporting our finding of "porous individualism" in which different pores become unstable at different imposed flow conditions.

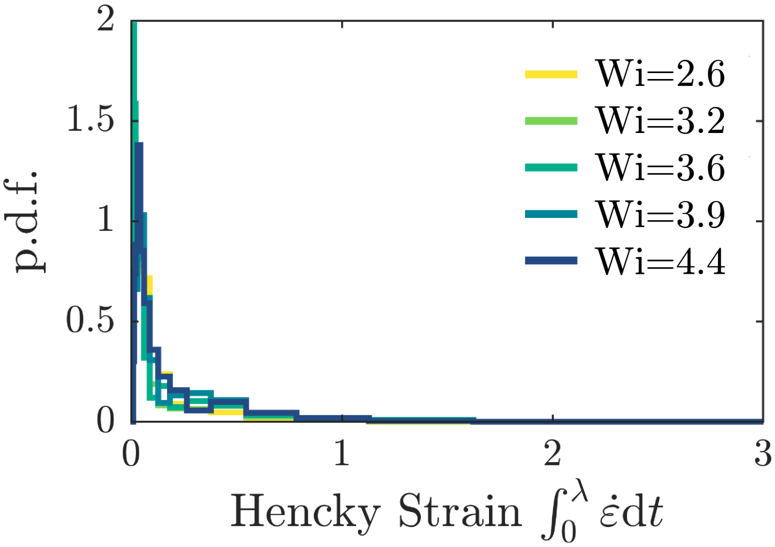

Figure S10: **Distribution of measured Hencky strains along sample pathlines of duration** $\lambda_0 \approx 1$ s. Colors indicate different macroscopic flow rates (reported as Wi_I). Distributions are taken over three pores, each with five sample track starting locations, and 15 time points with differing flow fields.

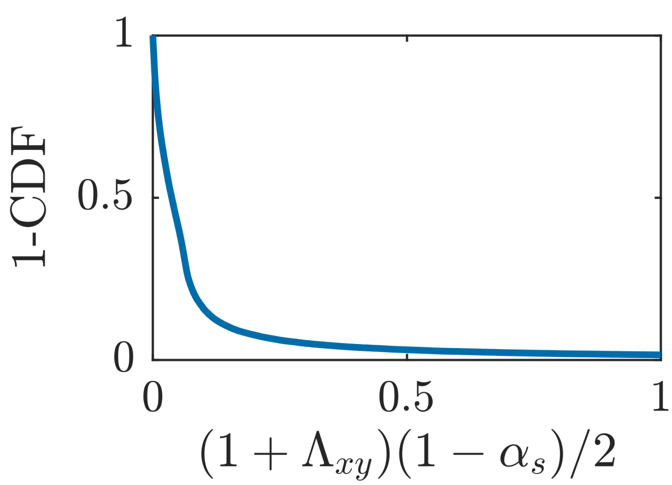

Figure S11: **Magnitude estimate of correctional term in simplified power balance**. The complementary cumulative distribution function of the in-plane component of the correctional term $(1 + \Lambda_{xy})(1 - \alpha_s)/2$, distributed over all tested flow rates and pixels. For a vast majority of pixels, the magnitude of this term is much less than 1. The average value of $\langle(1 + \Lambda_{xy})(1 - \alpha_s)/2\rangle_{v,Q} = 0.026 \ll 1$ indicates that $1 - (1 + \Lambda_{xy})(1 - \alpha_s)/2 \approx 1$.

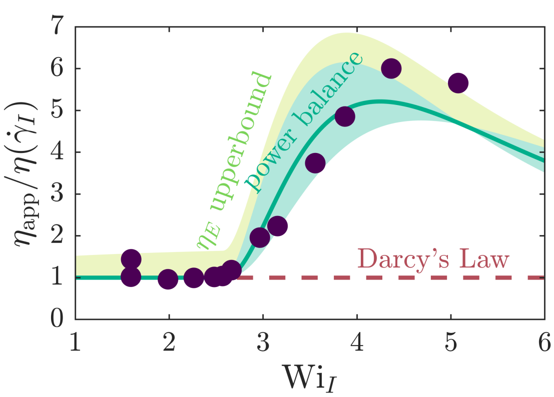

Figure S12: **Upper bound estimate of excess extensional viscous dissipation**. Reproduction of Fig. 4C, with added region to indicate upper bound expectation for the role of excess extensional viscous dissipation due to polymer elongation, as detailed in section B.6.

Pore name	**x (mm)**	**y (mm)**	Wi_c
A	58.52	2.99	2.62
B	60.55	2.79	3.11
C	59.88	0.65	3.56
D	1.36	2.34	3.53
E	1.55	2.04	3.13
F	1.02	1.94	3.94
G	1.31	1.78	2.90
H	60.93	3.05	3.23
I	59.93	2.30	3.13
J	59.74	1.71	3.11
K	59.82	1.01	3.92
L	59.57	0.70	4.02
M	61.10	1.01	-
N	0.65	2.65	-
O	1.55	1.55	-
P	1.24	1.35	-
Q	1.47	1.06	-
R	1.03	0.91	-
S	60.18	2.71	-
T	17.33	1.41	-
U	18.10	2.50	-

Table S1: **Additional data on pores selected for imaging**. Locations of the 19 pores (labeled A–S) selected at random throughout the medium for imaging and PIV. Positions are in reference to an arbitrary reference fiducial point. For pores with a well-defined onset, the fit Wi_c is given (see section A.3). Pores T and U are imaged continuously at select flow rates for Figs. S5–6 only, and are not used in any main text analysis. Locations for pores T and U are in reference to a different arbitrary reference fiducial point.

REFERENCES AND NOTES

1. M. M. Smith, J. A. Silva, J. Munakata-Marr, J. E. McCray, Compatibility of polymers and chemical oxidants for enhanced groundwater remediation. *Environ. Sci. Technol.* **42**, 9296–9301 (2008).

2. K. S. Sorbie, *Polymer-Improved Oil Recovery* (Springer Science & Business Media, 2013).

3. F. Durst, R. Haas, B. Kaczmar, Flows of dilute hydrolyzed polyacrylamide solutions in porous media under various solvent conditions. *J. Appl. Polym. Sci.* **26**, 3125–3149 (1981).

4. A. Bourgeat, O. Gipouloux, E. Marusic-Paloka, Filtration law for polymer flow through porous media. *Multiscale Model. Simul.* **1**, 432–457 (2003).

5. M. Luo, I. Teraoka, High osmotic pressure chromatography for large-scale fractionation of polymers. *Macromolecules* **29**, 4226–4233 (1996).

6. D. F. James, D. McLaren, The laminar flow of dilute polymer solutions through porous media. *J. Fluid Mech.* **70**, 733–752 (1975).

7. A. Clarke, A. M. Howe, J. Mitchell, J. Staniland, L. A. Hawkes, How viscoelastic-polymer flooding enhances displacement efficiency. *SPE J.* **21**, 0675–0687 (2016).

8. F. Durst, R. Haas, Dehnstrümungen mit verdünnten Polymerlüsungen: Ein theoretisches Modell und seine experimentelle Verifikation. *Rheol. Acta* **20**, 179–192 (1981).

9. N. Kauser, L. Dos Santos, M. Delgado, A. Muller, A. Saez, Flow of mixtures of poly(ethylene oxide) and hydrolyzed polyacrylamide solutions through porous media. *J. Appl. Polym. Sci.* **72**, 783–795 (1999).

10. R. Marshall, A. Metzner, Flow of viscoelastic fluids through porous media. *Ind. Eng. Chem. Fundam.* **6**, 393–400 (1967).

11. G. Chauveteau, M. Moan, The onset of dilatant behaviour in non-inertial flow of dilute polymer solutions through channels with varying cross-sections. *J. Phys. Lett.* **42**, 201–204 (1981).

12. S. J. Haward, J. A. Odell, Viscosity enhancement in non-Newtonian flow of dilute polymer solutions through crystallographic porous media. *Rheol. Acta* **42**, 516–526 (2003).

13. S. J. Haward, J. A. Odell, Viscosity enhancement in non-newtonian flow of dilute aqueous polymer solutions through crystallographic and random porous media. *Rheol. Acta* **45**, 853–863 (2006).

14. N. Zamani, I. Bondino, R. Kaufmann, A. Skauge, Effect of porous media properties on the onset of polymer extensional viscosity. *J. Pet. Sci. Eng.* **133**, 483–495 (2015).

15. A. Skauge, N. Zamani, J. Gausdal Jacobsen, B. Shaker Shiran, B. Al-Shakry, T. Skauge, Polymer flow in porous media: Relevance to enhanced oil recovery. *Colloids Interfaces* **2**, 27 (2018).

16. S. De, J. Kuipers, E. Peters, J. Padding, Viscoelastic flow simulations in random porous media. *J. Non-Newtonian Fluid Mech.* **248**, 50–61 (2017).

17. T. Burghelea, E. Segre, I. Bar-Joseph, A. Groisman, V. Steinberg, Chaotic flow and efficient mixing in a microchannel with a polymer solution. *Phys. Rev. E* **69**, 066305 (2004).

18. A. Machado, H. Bodiguel, J. Beaumont, G. Clisson, A. Colin, Extra dissipation and flow uniformization due to elastic instabilities of shear-thinning polymer solutions in model porous media. *Biomicrofluidics* **10**, 043507 (2016).

19. D. Kawale, E. Marques, P. L. Zitha, M. T. Kreutzer, W. R. Rossen, P. E. Boukany, Elastic instabilities during the flow of hydrolyzed polyacrylamide solution in porous media: Effect of pore-shape and salt. *Soft Matter* **13**, 765–775 (2017).

20. B. Qin, P. F. Salipante, S. D. Hudson, P. E. Arratia, Flow resistance and structures in viscoelastic channel flows at low Re. *Phys. Rev. Lett.* **123**, 194501 (2019).

21. R. G. Larson, E. S. Shaqfeh, S. J. Muller, A purely elastic instability in Taylor–Couette flow. *J. Fluid Mech.* **218**, 573–600 (1990).

22. E. S. Shaqfeh, Purely elastic instabilities in viscometric flows. *Annu. Rev. Fluid Mech.* **28**, 129–185 (1996).

23. P. Pakdel, G. H. McKinley, Elastic instability and curved streamlines. *Phys. Rev. Lett.* **77**, 2459–2462 (1996).

24. L. Rodd, J. Cooper-White, D. Boger, G. H. McKinley, Role of the elasticity number in the entry flow of dilute polymer solutions in micro-fabricated contraction geometries. *J. Non-Newtonian Fluid Mech.* **143**, 170–191 (2007).

25. A. Afonso, M. Alves, F. Pinho, Purely elastic instabilities in three-dimensional cross-slot geometries. *J. Non-Newtonian Fluid Mech.* **165**, 743–751 (2010).

26. J. Zilz, R. Poole, M. Alves, D. Bartolo, B. Levaché, A. Lindner, Geometric scaling of a purely elastic flow instability in serpentine channels. *J. Fluid Mech.* **712**, 203–218 (2012).

27. F. J. Galindo-Rosales, L. Campo-Deaño, F. Pinho, E. Van Bokhorst, P. Hamersma, M. S. Oliveira, M. Alves, Microfluidic systems for the analysis of viscoelastic fluid flow phenomena in porous media. *Microfluid. Nanofluid.* **12**, 485–498 (2012).

28. L. Pan, A. Morozov, C. Wagner, P. Arratia, Nonlinear elastic instability in channel flows at low Reynolds numbers. *Phys. Rev. Lett.* **110**, 174502 (2013).

29. V. Ribeiro, P. Coelho, F. Pinho, M. Alves, Viscoelastic fluid flow past a confined cylinder: Three-dimensional effects and stability. *Chem. Eng. Sci.* **111**, 364–380 (2014).

30. P. C. Sousa, F. T. Pinho, M. A. Alves, Purely-elastic flow instabilities and elastic turbulence in microfluidic cross-slot devices. *Soft Matter* **14**, 1344–1354 (2018).

31. C. A. Browne, A. Shih, S. S. Datta, Bistability in the unstable flow of polymer solutions through pore constriction arrays. *J. Fluid Mech.* **890**, A2 (2020).

32. C. A. Browne, A. Shih, S. S. Datta, Pore-scale flow characterization of polymer solutions in microfluidic porous media. *Small* **16**, 1903944 (2020).

33. A. Groisman, V. Steinberg, Elastic turbulence in a polymer solution flow. *Nature* **405**, 53–55 (2000).

34. J. Mitchell, K. Lyons, A. M. Howe, A. Clarke, Viscoelastic polymer flows and elastic turbulence in three-dimensional porous structures. *Soft Matter* **12**, 460–468 (2016).

35. D. M. Walkama, N. Waisbord, J. S. Guasto, Disorder suppresses chaos in viscoelastic flows. *Phys. Rev. Lett.* **124**, 164501 (2020).

36. S. J. Haward, C. C. Hopkins, A. Q. Shen, Stagnation points control chaotic fluctuations in viscoelastic porous media flow. *Proc. Natl. Acad. Sci. U.S.A.* **118**, e2111651118 (2021).

37. M. J. Blunt, *Multiphase Flow in Permeable Media: A Pore-Scale Perspective* (Cambridge Univ. Press, 2017).

38. F. Zami-Pierre, R. De Loubens, M. Quintard, Y. Davit, Transition in the flow of power-law fluids through isotropic porous media. *Phys. Rev. Lett.* **117**, 074502 (2016).

39. S. Berg, J. van Wunnik, Shear rate determination from pore-scale flow fields. *Transp. Porous Media* **117**, 229–246 (2017).

40. B. Qin, P. E. Arratia, Characterizing elastic turbulence in channel flows at low Reynolds number. *Phys. Rev. Fluids* **2**, 083302 (2017).

41. G. Lemoult, L. Shi, K. Avila, S. V. Jalikop, M. Avila, B. Hof, Directed percolation phase transition to sustained turbulence in Couette flow. *Nat. Phys.* **12**, 254–258 (2016).

42. C. Letellier, Intermittency as a transition to turbulence in pipes: The long tradition from Reynolds to the 21st century. *Mech. Rep.* **345**, 642–659 (2017).

43. D. Barkley, Theoretical perspective on the route to turbulence in a pipe. *J. Fluid Mech.* **803**, 1–80 (2016).

44. R. van Buel, C. Schaaf, H. Stark, Elastic turbulence in two-dimensional Taylor-Couette flows. *Europhys. Lett.* **124**, 14001 (2018).

45. P. De Gennes, Molecular individualism. *Science* **276**, 1999–2000 (1997).

46. Additional details of the analysis of pore-scale flow fields, supplementary figures, and captions for supplementary movies are given in the Supplementary Materials.

47. R. B. Bird, R. C. Armstrong, O. Hassager, *Dynamics of Polymeric Liquids. Vol. 1: Fluid Mechanics* (John Wiley and Sons, 1987).

48. G. H. McKinley, T. Sridhar, Filament-stretching rheometry of complex fluids. *Annu. Rev. Fluid Mech.* **34**, 375–415 (2002).

49. S. B. Pope, *Turbulent Flows* (Cambridge Univ. Press, 2012).

50. A. M. Howe, A. Clarke, D. Giernalczyk, Flow of concentrated viscoelastic polymer solutions in porous media: Effect of MW and concentration on elastic turbulence onset in various geometries. *Soft Matter* **11**, 6419–6431 (2015).

51. L. Xi, M. D. Graham, Intermittent dynamics of turbulence hibernation in Newtonian and viscoelastic minimal channel flows. *J. Fluid Mech.* **693**, 433–472 (2012).

52. C. Scholz, F. Wirner, J. R. Gomez-Solano, C. Bechinger, Enhanced dispersion by elastic turbulence in porous media. *Europhys. Lett.* **107**, 54003 (2014).

53. P. Ligrani, D. Copeland, C. Ren, M. Su, M. Suzuki, Heat transfer enhancements from elastic turbulence using sucrose-based polymer solutions. *J. Thermophys. Heat Transf.* **32**, 51–60 (2018).

54. X. Wang, M. Jiang, Z. Zhou, J. Gou, D. Hui, 3d printing of polymer matrix composites: A review and prospective. *Compos. Part B Eng.* **110**, 442–458 (2017).

55. S. S. Datta, H. Chiang, T. Ramakrishnan, D. A. Weitz, Spatial fluctuations of fluid velocities in flow through a three-dimensional porous medium. *Phys. Rev. Lett.* **111**, 064501 (2013).

56. A. T. Krummel, S. S. Datta, S. Münster, D. A. Weitz, Visualizing multiphase flow and trapped fluid configurations in a model three-dimensional porous medium. *AICHE J.* **59**, 1022–1029 (2013).

57. A. P. Philipse, C. Pathmamanoharan, Liquid permeation (and sedimentation) of dense colloidal hard-sphere packings. *J. Colloid Interface Sci.* **159**, 96–107 (1993).

58. W. W. Graessley, Polymer chain dimensions and the dependence of viscoelastic properties on concentration, molecular weight and solvent power. *Polymer* **21**, 258–262 (1980).

59. M. Rubinstein, R. H. Colby, *Polymer Physics* (Oxford Univ. Press, 2003).

60. H. Zhang, Y. Feng, Dependence of intrinsic viscosity and molecular size on molecular weight of partially hydrolyzed polyacrylamide. *J. Appl. Polym. Sci.* **138**, 50850 (2021).

61. S. A. Vanapalli, S. L. Ceccio, M. J. Solomon, Universal scaling for polymer chain scission in turbulence. *Proc. Natl. Acad. Sci. U.S.A.* **103**, 16660–16665 (2006).

62. W. Thielicke, E. J. Stamhuis, Pivlab—Towards user-friendly, affordable and accurate digital particle image velocimetry in MATLAB. *J. Open Res. Softw.* **2**, e30 (2014).

63. A. Groisman, V. Steinberg, Elastic turbulence in curvilinear flows of polymer solutions. *New J. Phys.* **6**, 29 (2004).

64. G. Vinogradov, V. Manin, An experimental study of elastic turbulence. *Kolloid Z. Z. Polym.* **201**, 93–98 (1965).

65. N. K. Jha, V. Steinberg, Universal coherent structures of elastic turbulence in straight channel with viscoelastic fluid flow. arXiv:2009.12258 [physics.flu-dyn] (25 September 2020).

66. R. van Buel, H. Stark, Active open-loop control of elastic turbulence. *Sci. Rep.* **10**, 15704 (2020).

67. D. J. Ruth, W. Mostert, S. Perrard, L. Deike, Bubble pinch-off in turbulence. *Proc. Natl. Acad. Sci. U.S.A.* **116**, 25412–25417 (2019).

68. G. H. McKinley, P. Pakdel, A. Öztekin, Rheological and geometric scaling of purely elastic flow instabilities. *J. Non-Newtonian Fluid Mech.* **67**, 19–47 (1996).

69. L. E. Rodd, T. P. Scott, D. V. Boger, J. J. Cooper-White, G. H. McKinley, The inertio-elastic planar entry flow of low-viscosity elastic fluids in micro-fabricated geometries. *J. Non-Newtonian Fluid Mech.* **129**, 1–22 (2005).

70. Y. Lam, H. Gan, N.-T. Nguyen, H. Lie, Micromixer based on viscoelastic flow instability at low Reynolds number. *Biomicrofluidics* **3**, 014106 (2009).

71. N. P. Teclemariam, V. A. Beck, E. S. Shaqfeh, S. J. Muller, Dynamics of DNA polymers in post arrays: Comparison of single molecule experiments and simulations. *Macromolecules* **40**, 3848–3859 (2007).

72. A. Lanzaro, X.-F. Yuan, Effects of contraction ratio on non-linear dynamics of semi-dilute, highly polydisperse PAAm solutions in microfluidics. *J. Non-Newtonian Fluid Mech.* **166**, 1064–1075 (2011).

73. A. Lanzaro, X.-F. Yuan, A quantitative analysis of spatial extensional rate distribution in nonlinear viscoelastic flows. *J. Non-Newtonian Fluid Mech.* **207**, 32–41 (2014).

74. A. Lanzaro, Z. Li, X.-F. Yuan, Quantitative characterization of high molecular weight polymer solutions in microfluidic hyperbolic contraction flow. *Microfluid. Nanofluid.* **18**, 819–828 (2015).

75. A. Lanzaro, D. Corbett, X.-F. Yuan, Non-linear dynamics of semi-dilute PAAm solutions in a microfluidic 3d cross-slot flow geometry. *J. Non-Newtonian Fluid Mech.* **242**, 57–65 (2017).

76. B. Qin, P. F. Salipante, S. D. Hudson, P. E. Arratia, Upstream vortex and elastic wave in the viscoelastic flow around a confined cylinder. *J. Fluid Mech.* **864**, R2 (2019).

77. D. Kawale, G. Bouwman, S. Sachdev, P. L. Zitha, M. T. Kreutzer, W. R. Rossen, P. E. Boukany, Polymer conformation during flow in porous media. *Soft Matter* **13**, 8745–8755 (2017).

78. A. Varshney, V. Steinberg, Elastic wake instabilities in a creeping flow between two obstacles. *Phys. Rev. Fluids* **2**, 051301 (2017).

79. S. Kenney, K. Poper, G. Chapagain, G. F. Christopher, Large Deborah number flows around confined microfluidic cylinders. *Rheol. Acta* **52**, 485–497 (2013).

80. X. Shi, S. Kenney, G. Chapagain, G. F. Christopher, Mechanisms of onset for moderate mach number instabilities of viscoelastic flows around confined cylinders. *Rheol. Acta* **54**, 805–815 (2015).

81. X. Shi, G. F. Christopher, Growth of viscoelastic instabilities around linear cylinder arrays. *Phys. Fluids* **28**, 124102 (2016).

82. A. Groisman, V. Steinberg, Efficient mixing at low Reynolds numbers using polymer additives. *Nature* **410**, 905–908 (2001).

83. S. J. Haward, G. H. McKinley, A. Q. Shen, Elastic instabilities in planar elongational flow of monodisperse polymer solutions. *Sci. Rep.* **6**, 33029 (2016).

84. J. A. Byars, "Experimental characterization of viscoelastic flow instabilities," thesis, Massachusetts Institute of Technology (1996).

85. R. B. Bird, W. E. Stewart, E. N. Lightfoot, *Transport Phenomena* (John Wiley and Sons, 1960).

86. S. Whitaker, *Introduction to Fluid Mechanics* (Krieger Pub. Co., 1992).

87. A. Delafosse, M.-L. Collignon, M. Crine, D. Toye, Estimation of the turbulent kinetic energy dissipation rate from 2d-piv measurements in a vessel stirred by an axial mixel ttp impeller. *Chem. Eng. Sci.* **66**, 1728–1737 (2011).

88. K. V. Sharp, K. C. Kim, R. Adrian, *Laser Techniques Applied to Fluid Mechanics* (Springer, 2000), pp. 337–354.